

Article

# Numerical Modeling of Solitary Wave-Induced Flow and Scour around a Square Onshore Structure

Jinzhao Li <sup>1</sup>, Xuan Kong <sup>1,\*</sup> , Yilin Yang <sup>2</sup>, Jiexuan Hu <sup>1</sup> and Ruijia Jin <sup>3</sup>

<sup>1</sup> Key Laboratory for Damage Diagnosis of Engineering Structures of Hunan Province, College of Civil Engineering, Hunan University, Changsha 410082, China

<sup>2</sup> School of Civil Engineering, Central South University, Changsha 410083, China

<sup>3</sup> National Engineering Laboratory for Port Hydraulic Construction Technology, Tianjin Research Institute for Water Transport Engineering, M.O.T., Tianjin 300456, China

\* Correspondence: kongxuan@hnu.edu.cn

**Abstract:** Waves or tsunamis in the onshore area could induce severe scour at the structure foundations, threatening the stability of the structure. This paper presents a numerical study of the solitary wave-induced flow and scour around a square onshore structure. A CFD model coupled with hydrodynamic and sediment transport models is first validated through a large-scale laboratory experiment, which shows that the model can well reproduce the flow and scour characteristics. Subsequently, based on the reliable numerical results, the flow field and scour development during wave inundation of the structure are explored. It is found that the development of the simulated scour depth is faster at the early stage compared to that in the experimental result. The results also show that the scour starts at the front corner of the structure, which is also the position of the maximum scour depth. The scour develops rapidly at the early stage and is almost completed in the first half of the wave period. In addition, the results demonstrate that bed scouring increases the wave force on the structure due to the increase in the flow velocity near the bed, which needs to be considered, especially in the shallow-water scour scenario. Finally, a simplified prediction equation is proposed for the temporal development of the scour depth.

**Keywords:** numerical modeling; CFD; scour; solitary wave; onshore structure; wave force



**Citation:** Li, J.; Kong, X.; Yang, Y.; Hu, J.; Jin, R. Numerical Modeling of Solitary Wave-Induced Flow and Scour around a Square Onshore Structure. *J. Mar. Sci. Eng.* **2023**, *11*, 198. <https://doi.org/10.3390/jmse11010198>

Academic Editor: María Isabel Lamas Galdo

Received: 15 December 2022

Revised: 4 January 2023

Accepted: 6 January 2023

Published: 12 January 2023



**Copyright:** © 2023 by the authors. Licensee MDPI, Basel, Switzerland. This article is an open access article distributed under the terms and conditions of the Creative Commons Attribution (CC BY) license (<https://creativecommons.org/licenses/by/4.0/>).

## 1. Introduction

In the past decades, more and more structures (e.g., breakwaters or bridges) and buildings have been built in the onshore area. Many of these structures are constructed with vertical square foundations which are inevitably subjected to waves, and, in extreme conditions, these onshore structures could be damaged devastatingly by a huge attack from a tsunami or storm surge. The waves or tsunamis impacting the structure can induce severe scour around its foundation, which undermines the stability of the structure [1–3]. Therefore, to ensure the safety of the onshore structure, it is crucial to improve our understanding of the foundation scour and further make a reliable estimation of the scour depth.

Extensive studies on the subject of scour around marine structures have been reported (see the review by Sumer and Kirca (2021) [4]). Most of the previous studies concern structures located in offshore conditions. Compared to an offshore structure in a deep-water environment, the onshore environment is characterized by shallow-water conditions in which the scour characteristics are different in two ways: (i) The onshore area is an active zone of sediment movement and morphology change, as most of the energy of the waves on the free surface directly contributes to the seabed, and thus the scour around the structure develops more rapidly and behaves more like a transient process [5]. (ii) The wave condition in the onshore area is more complicated, including wave shoaling and even breaking, which results in that the flow and scour mechanism around the structure differs from the offshore scour [6]. However, studies of scour involving a square onshore structure

are quite limited. The most relevant study is by McGovern et al. (2019) [7], who investigated the scour around a square onshore structure induced by tsunami-length long waves. That is also the first experimental study that considers tsunami inundation time-scales appropriate to prototype. Similarly, Mehrzad et al. (2022) [8] experimentally studied the mechanism of scour around a square structure induced by a tsunami-like bore. They found that the high velocity and relatively short duration of a tsunami-like bore can induce rapid scour around the structure. In addition, Xu et al.'s (2022) [9] study shows that the seabed scour can increase the wave force on the onshore structure, as the scouring increases the local water depth and changes the hydrodynamic conditions around the structure. They also suggested that the reasonable design of onshore structures needs to adequately consider seabed scour and the associated increase in wave force.

The aforementioned experimental studies not provide insight into this issue but also supply some valuable experimental data. However, the experiment is expensive because normally a large wave flume is required to generate the long waves and reduce the scaling effect as much as possible [10]. Moreover, although some illuminating phenomena have been observed qualitatively in the experiment, more details on the flow and scour characteristics are absent due to the limitations of the measuring equipment. With the development of the modern computational fluid dynamics (CFD) method, the CFD-based flow model incorporating sediment transport and morphological models has been successfully used to study the wave-induced scour around structures (e.g., [11–21]). For the sake of space limitations, for more details on the recent development of CFD modeling of scour around marine structures, the readers are referred to the recent reviews [22,23]. The CFD modeling approach has the advantage of obtaining abundant data or information (e.g., a detailed description of flow field and scour morphology), which is helpful in elucidating the underlying mechanism of this scour issue.

The aim of this study is to identify the flow and scour mechanisms during the process of the wave inundation of the square onshore structure based on a reliable CFD model. The rest of this article is organized as follows: The fully-coupled numerical model is described in Section 2. In Section 3, the numerical setup is presented, and the model is validated through comparison with the available experimental results. Section 4 shows the numerical results of the flow characteristics, wave force, and scour evolution, and a simple predictive equation for the temporal development of the scour depth is proposed. Conclusions are given in Section 5.

## 2. Numerical Model Description

### 2.1. Hydrodynamic Model

In this study, the wave-induced scour around the onshore structure is simulated utilizing the CFD software *FLOW-3D* v11.2.0. The hydrodynamic model is based on the incompressible unsteady Reynolds-Averaged Navier-Stokes (RANS) equations, as shown in the following:

$$\frac{\partial u_i}{\partial t} + u_j \frac{\partial u_i}{\partial x_j} = -\frac{1}{\rho} \frac{\partial p}{\partial x_i} + \frac{\partial}{\partial x_j} \left[ 2\nu S_{ij} + \frac{\tau_{ij}}{\rho} \right] + \frac{\sigma_T \kappa \gamma}{\rho} \frac{\partial \gamma}{\partial x_i} \quad (1)$$

$$\frac{\partial u_i}{\partial x_i} = 0 \quad (2)$$

where  $u_i$  and  $u_j$  are the velocity components in the  $i$ th and  $j$ th Cartesian coordinates,  $p$  is the pressure,  $\nu$  is the dynamic viscosity, and  $\rho$  is the fluid density.  $S_{ij}$  is the mean strain rate tensor defined as

$$S_{ij} = \frac{1}{2} \left( \frac{\partial u_i}{\partial x_j} + \frac{\partial u_j}{\partial x_i} \right) \quad (3)$$

and  $\tau_{ij}$  is the Reynolds stress tensor, which is calculated based on the Boussinesq approximation:

$$\tau_{ij} = -\overline{u'_i u'_j} = 2\nu_T S_{ij} - \frac{2}{3} k \delta_{ij} \quad (4)$$

where  $\delta_{ij}$  is the Kronecker delta,  $\nu_T$  is the turbulent kinematic viscosity, and  $k$  is the turbulent kinetic energy defined as

$$k = \frac{1}{2} \overline{u'_i u'_i} \tag{5}$$

where the overbar denotes ensemble averaging. The last term in Equation (1) is the effect of the water surface tension, where  $\sigma_T$  is the surface tension coefficient,  $\kappa_\gamma$  is the surface curvature, and  $\gamma$  is the indicator representing the volume fraction, which takes a value 0 in air, 1 in water, and 0–1 in an air-water mixture. In terms of  $\gamma$ , one can express the spatial variation in any fluid property, such as  $\rho$  and  $\nu$ , through the weighting

$$\phi = \gamma \phi_{\text{water}} + (1 - \gamma) \phi_{\text{air}} \tag{6}$$

where  $\phi$  can be any such quantity.

The  $k$ - $\omega$  turbulence model [24] is employed and formulated as

$$\frac{\partial k}{\partial t} + u_j \frac{\partial k}{\partial x_j} = \frac{\tau_{ij}}{\rho} \frac{\partial u_i}{\partial x_j} - \beta^* k \omega + \frac{\partial}{\partial x_j} \left[ \left( \nu + \sigma^* \frac{k}{\omega} \right) \frac{\partial k}{\partial x_j} \right] \tag{7}$$

$$\frac{\partial \omega}{\partial t} + u_j \frac{\partial \omega}{\partial x_j} = \alpha \frac{\omega}{k} \frac{\tau_{ij}}{\rho} \frac{\partial u_i}{\partial x_j} - \beta \omega^2 + \frac{\sigma_d}{\omega} \frac{\partial k}{\partial x_j} \frac{\partial \omega}{\partial x_j} + \frac{\partial}{\partial x_j} \left[ \left( \nu + \sigma \frac{k}{\omega} \right) \frac{\partial \omega}{\partial x_j} \right] \tag{8}$$

$$\nu_T = \frac{k}{\omega}, \quad \omega = \max \left\{ \omega, C_{lim} \sqrt{\frac{2S_{ij}S_{ij}}{\beta^*}} \right\} \tag{9}$$

$$\sigma_d = H \left\{ \frac{\partial k}{\partial x_j} \frac{\partial \omega}{\partial x_j} \right\} \sigma_{do} \tag{10}$$

where  $\omega$  is the specific dissipation rate,  $C_{lim} = 7/8$  is a stress limiting coefficient, and  $H\{\cdot\}$  is the Heaviside step function, taking a value of zero if the argument is negative and unity otherwise. The default values of the model coefficients  $\alpha = 0.52$ ,  $\beta = 0.078$ ,  $\beta^* = 0.09$ ,  $\sigma = 0.5$ ,  $\sigma^* = 0.6$ , and  $\sigma_{do} = 0.125$  are adopted.

The hydrodynamic model described above is subject to the following boundary conditions. At the bottom wall boundaries, a no-slip condition is imposed whereby velocities are set to zero. Alternatively, Neumann conditions are applied to the three components of the velocity and scalar hydrodynamic quantities at the two lateral side boundaries. At the inlet boundary, a solitary wave is prescribed by using its analytical expression. An outflow boundary is used at the outlet. At the top free surface, a volume of fluid (VOF) method is used to model the water-air interface, which will be presented in the forthcoming section.

### 2.2. Free Surface Model and Wave Generation

The free surface (water-air interface) is tracked by the commonly-used VOF method depending on the volume fraction  $\gamma$ , which can be solved by an advection equation:

$$\frac{\partial \gamma}{\partial t} + \frac{\partial \gamma u_j}{\partial x_j} = 0 \tag{11}$$

In this study, waves are generated at the inlet boundary, and the solitary wave is used to simulate a wave propagating over the nearshore area. As the shape of a solitary wave is reasonably similar to that of the wind waves near the coast, it has been commonly used in studies related to coastal hydrodynamics.

### 2.3. Sediment Transport and Morphological Models

The sediment transport model is classified into bed load and suspended load sediment transport. The bed load sediment transport  $q_b$  is determined via the van Rijn equation:

$$q_b = 0.053 \left[ g(s - 1)d_{50}^3 \right]^{1/2} (\theta - \theta_c)^{2.1} (d^*)^{-0.3} \tag{12}$$

where  $d_{50}$  is the median diameter of the sediment particles,  $s = \rho_s/\rho$  is the sediment relative density, and  $\theta$  is the Shields number defined as:

$$\theta = \frac{U_f^2}{(s - 1)gd_{50}} \tag{13}$$

where  $U_f$  is the friction velocity. The critical Shields parameter  $\theta_c$  is determined by the following equation:

$$\theta_c = \frac{0.3}{1 + 1.2d_*} + 0.055[1 - \exp(-0.02d_*)] \tag{14}$$

where  $d_*$  is the dimensionless sediment size and can be determined by

$$d_* = \left[ g(s - 1)/\nu^2 \right]^{1/3} d_{50} \tag{15}$$

The suspended sediment concentration is obtained by solving the following convection-diffusion equation:

$$\frac{\partial c}{\partial t} + (u_j - w_s \delta_{j3}) \frac{\partial c}{\partial x_j} = \frac{\partial}{\partial x_j} \left[ (v + \nu_T) \frac{\partial c}{\partial x_j} \right] \tag{16}$$

where  $c$  is the mass concentration of suspended sediment particles, and  $w_s$  is the particle fall velocity.

At all boundaries for the sediment model except for the bottom boundary, a zero-flux condition for  $c$  is used. At the bottom boundary, so-called reference concentration boundary conditions are imposed, which is in line with the approach in [5].

The morphological model is based on the sediment continuity (Exner) equation:

$$\frac{\partial z_b}{\partial t} = \frac{1}{(n - 1)} \frac{\partial q_{bi}}{\partial x_i} + (D_s - E_s) \tag{17}$$

where the left hand term represents the change of bed elevation  $z_b$ . At the right hand side of the equation, the first term is the contribution from the bed load transport  $q_{bi}$ ,  $n = 0.4$  is the sediment porosity, and the second term is the contribution from the suspended load transport, in which  $(E_s - D_s)$  represents the net sediment quantity between sediment erosion and deposition. For more specific details on the numerical solution, the readers can refer the previously published paper by the authors [19].

## 3. Model Validation

### 3.1. Numerical Setup

The present numerical case is identical to that of McGovern et al.'s (2019) [7] experiment conducted in a large-scale flume of 75 m in length, 3 m in width, and 2.5 m in height. As shown in the following sketch in Figure 1, a generated solitary wave propagates along a flume with a constant water depth (23.9 m long) followed by a 1/20 sloping beach, before impinging on and inundating a 3 m long horizontal sediment bed. Uniform sediment ( $d_{50} = 0.16$  mm and  $\rho_s = 2.643 \times 10^3$  kg/m<sup>3</sup>) was used in the experiment. A 0.2 m wide square structure was placed at the sediment pit, which can be considered as about a

1/10 prototype scale based on Froude similitude. One of the tests in the experiments of [7] (i.e., CL25a run) was selected, and the detailed test conditions are listed in Table 1.

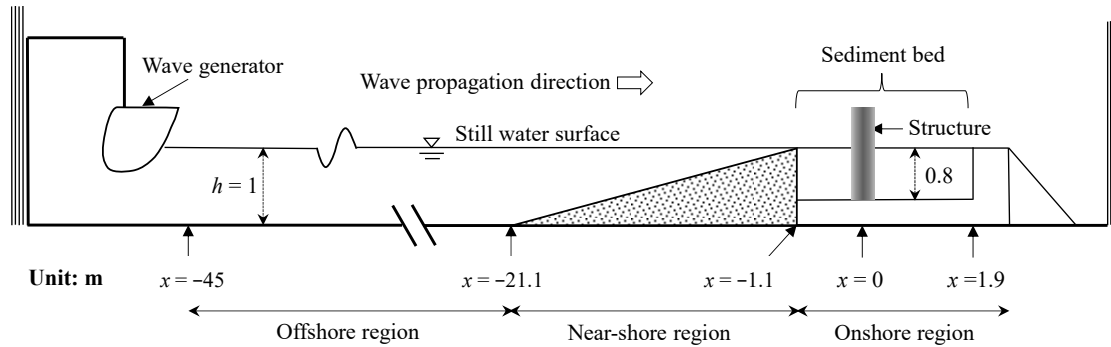


Figure 1. The wave flume and experimental setup [7] used for validation.

Table 1. Test conditions in the numerical simulation:  $h$ , water depth;  $H$ , wave height;  $T$ , wave period;  $U_m$ , maximum value of depth-averaged velocity;  $D$ , structure width;  $d_{50}$ , sediment size,  $KC = U_m T / D$ , Keulegan-Carpenter number;  $Fr = U_m / (gh)^{0.5}$ , Froude number.

$h$ [m]	$H$ [m]	$T$ [s]	$U_m$ [m/s]	$D$ [m]	$d_{50}$ [mm]	$KC$ [-]	$Fr$ [-]
1.00	0.11	25	0.67	0.20	0.16	83	0.47

Figure 2 presents the computational domain and mesh of the numerical modeling. The present numerical simulation is a three-dimensional case, and the setup of the computational domain is the same as for the laboratory flume mentioned above. Since the solitary wave used in the present case has a large wavelength, a long computational domain before the structure is required for the wave generation and development. The origin of the coordinate system is defined at the center of the structure bottom, with the longitudinal  $x$ -axis parallel to the flume bed and pointing onshore, the  $y$ -axis normal to the side wall of the flume, and  $z$ -axis vertically normal to the bottom of the flume. The computational domain is divided into several mesh regions with varying grid resolutions. The grids in the range from the inlet to the toe of the slope are relatively coarse as long as the wave propagation is well reproduced before arriving at the onshore region. Meanwhile, the grids within the onshore region are gradually refined, and the finest meshes are required close to the pile, specifically with at least 20 grids at each face of the structure (see the top view), and the near-bed cell, having a height in the order of the grain size (see the side view). This can guarantee the capture of the details of the flow and scour around the pile. In fact, the mesh sensitivity has been calibrated to obtain the optimal mesh while keeping the computational time affordable.

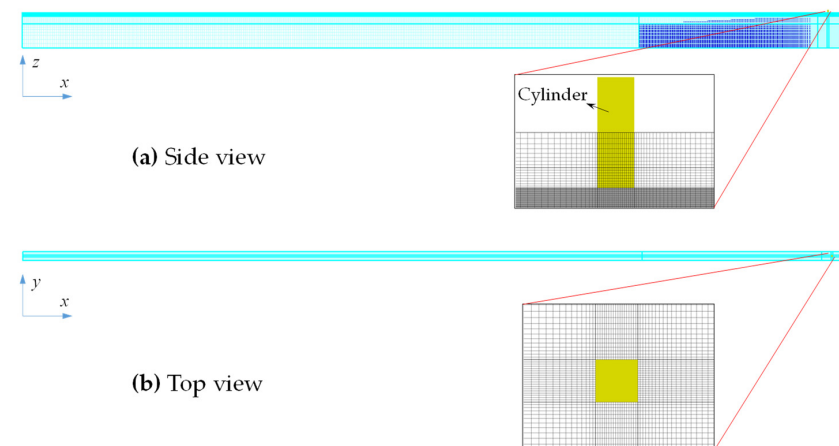


Figure 2. Computational mesh setup and the local refined grid in the vicinity of structure.

The boundary conditions of the computational domain are as follows. The top and two sides of the domain are set as symmetry boundaries, which is an advisable strategy for improving the computation efficiency. The wall boundary condition is specified at the bottom and at the structure surface, and the standard wall function approach is utilized to determine the friction velocity [5]. For the wave boundary at the inlet, the solitary wave is generated by prescribing the analytical free surface  $\eta$  profile of the solitary wave:

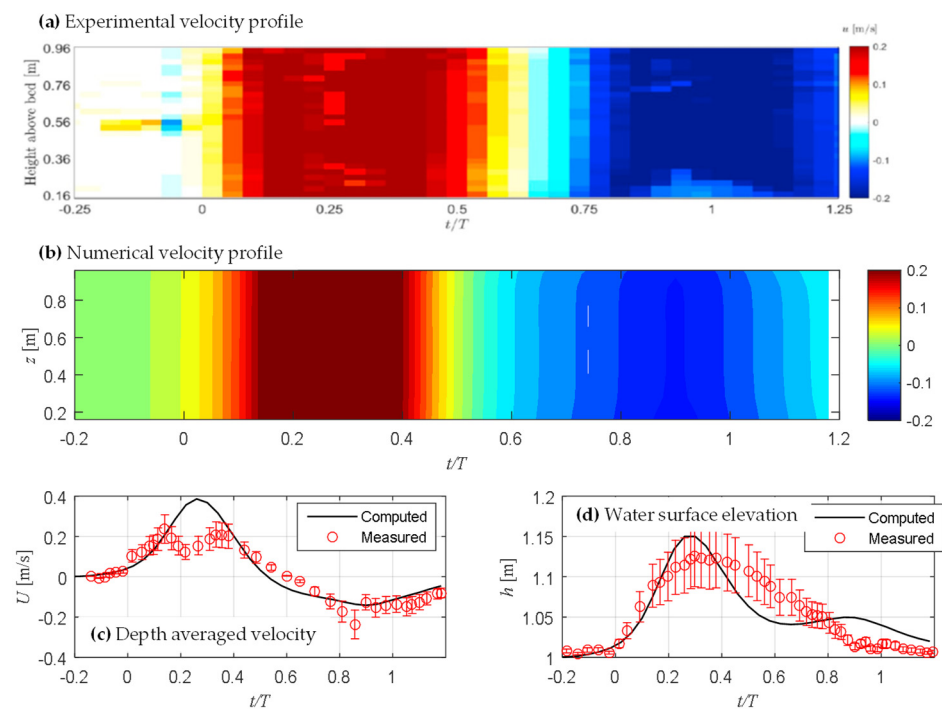
$$\eta = H \operatorname{sech}^2 \left[ \sqrt{\frac{3H}{4h^3}} (x - c_w t) \right] \quad (18)$$

where  $c_w$  is the wave celerity. For the outlet of the domain, an outflow boundary condition is used.

As an indication of the computational expense, the fully-coupled hydrodynamic and morphological computation lasting 1 min of physical time for the present scour cases requires approximately 5 days of CPU time, when simulated in parallel on twenty modern processors. To give an indication of the CPU times, the authors would like to note that, for the same computational mesh and using the same computational power, the hydrodynamic computations alone for 1 min of physical time last approximately 0.5 days, and 1.5 days if the sediment computations are also included. Throughout the study, it has been seen that the morphological computations have governed the speed of the simulations. It is worth noting that efforts were made to simulate this scour issue in large scale, and the present simulation is a 1/10 scaling model based on Froude similitude. To the best of our knowledge, it is the first time that such a large-scale scour simulation has been created.

### 3.2. Comparison with Experimental Results

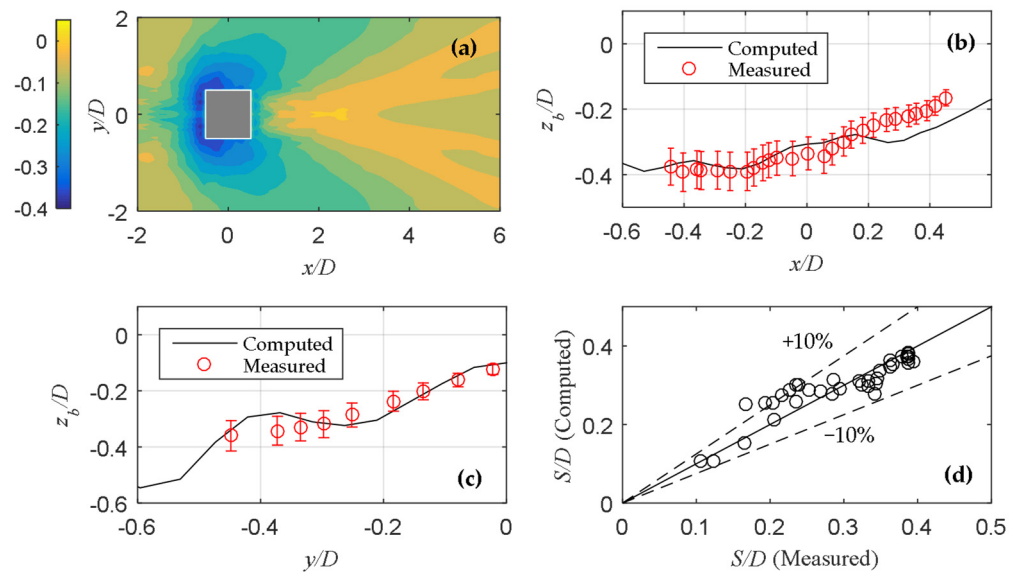
In this section, the numerical simulated results are compared with the experimentally measured data to validate the present CFD model. Figure 3 presents the comparisons of the flow characteristics, including the water surface elevation and velocity. The temporal variation of the velocity profile in the vertical direction (Figure 3a,b) indicates that both the experimental and the numerical results are quite similar, based on the distribution of color. To further verify the numerical results, Figure 3c,d quantitatively compare the time histories of the depth-averaged velocity and water elevation at the slope toe. The black solid lines and red dots represent the computed and measured results, respectively. The 20% error bars are also plotted in the experimental data. They show that the CFD simulated results fit well with the experimental data except for the peak value of the velocity. The reasons for the discrepancies are twofold. (i) The complexity of the physical process, involving wave transforming, shoaling, or even breaking, increases the uncertainty of the velocity measurement, especially for the wave peak phase. (ii) In the experiment, the velocity profile was measured by a Nortek HR Aquadopp, which could result in some uncertainty and error, and this can be seen in Figure 3a, in which the velocity contour is not as smooth as the numerical result. In addition, the deviation in the water surface elevation (Figure 3d) is mainly attributed to the solitary wave generated by the wave maker. Through the inspection of the generated wave in the experiment (see the figure in [7]), it is observed that the generated wave is not exactly consistent to the theoretical solitary waveform, particularly as it has some obvious trailing waves, whereas, in the numerical modeling, the theoretical wave form can be easily generated by setting the inlet boundary condition. In general, although the present numerical simulated result is not perfect, it should be admitted that accurately modeling such complicated cases (involving wave transforming, shoaling, and breaking, and the associated bed scour) is still a challenging task.



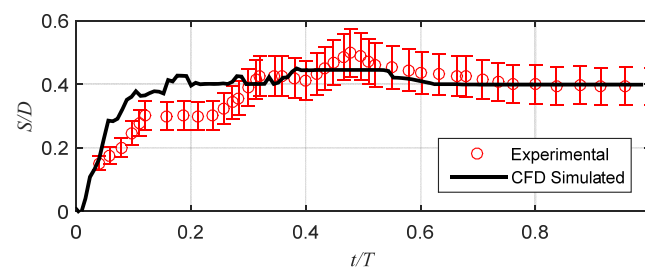
**Figure 3.** Comparison of flow characteristics at the slope toe between CFD computed and experimentally measured results: (a,b) temporal variation of velocity profile; (c) time history of depth-averaged velocity; (d) time history of water surface elevation.

Figure 4 shows the comparisons of local scour around the structure according to the CFD simulated and the experimentally measured results. Figure 4a–c plot the final scour morphology and scoured bed profile. The 20% error bars are plotted in the experimental data. The numerical results indicate that the maximum scour depth is located at the front corner of the square structure, which is consistent with the experimental observations. Further comparison of the scoured bed profile, whether in the longitudinal or transverse direction, demonstrates that the CFD modeling replicates the experimental results well. Figure 4b exhibits some deviations in the zone of  $x/D > 0.3$ . This is probably due to the sand slide model employed in the sediment transport model. To ensure that the bed slopes do not exceed the angle of repose, a sand slide model is utilized. Although this strategy is used for the purpose of avoiding some unphysical large bed slope during scour simulation, some uncertainties and errors, e.g., non-conservation of sediment mass, would occur [25]. Nevertheless, the maximum scour depth, which is always concerned as a critical index in practical engineering, is well simulated by the present CFD model. From Figure 4d, in which the data of scour depth is plotted and compared, the accuracy of the CFD modeling is clearly verified, with almost all the data falling within the  $\pm 10\%$  error lines.

Figure 5 also shows the comparison of scour depth development with time at the front corner of the structure, for which both the simulated and measured profiles agree well, except for the early stage ( $t/T < 0.3$ ), in which the simulated scour rate is higher. This result is also consistent with the previous relevant simulations [16]. The reasons can be illustrated by two aspects. (i) The vortex of the flow field around the structure cannot be well captured by the RANS model, and this is a general problem in RANS simulation [22]. (ii) The sediment transport model used in the present scour simulation does not consider the influence of turbulence (see more discussion in our previous paper [26]).



**Figure 4.** Comparisons of local scour around structure between CFD simulated and experimental measured results: (a) final bed elevation contour; (b) final scour bed profile along longitudinal direction; (c) final scour bed profile along transverse direction; (d) comparison between computed and measured scour depth.



**Figure 5.** Comparison of scour depth development at the front corner position between CFD simulated and experimental measured results.

Overall, based on the previous comparisons, the present CFD model can well reproduce the solitary wave-induced flow and scour characteristics around the structure, including the scour depth development and the final scour profile. Hence, the validated CFD model (which offers the advantage of obtaining more abundant results compared to the experiment) can be used as a promising tool to explore the fundamental mechanism of the scour, which will be presented in the following sections.

#### 4. Numerical Results and Discussion

Based on the reliable simulated results, which have been thoroughly validated above, some hydrodynamic and scour characteristics observed during the process of wave inundation of the structure are described and discussed, including the free surface evolution around the structure, flow velocity variation, wave force acting on the structure, and scour development. Furthermore, a practical equation to predict the temporal development of the scour depth is proposed.

##### 4.1. Flow and Scour Processes

Figure 6 shows the time history of the free surface elevation in front of the structure during the process of wave inundation of the structure. Four typical moments are plotted ( $t_1 \sim t_4$ ), corresponding to the phases of wave run-up, peak run-up, wave draw-down, and trailing. The three-dimensional views of the water surface evolution around the structure at these typical moments ( $t_1 \sim t_4$ ) are presented in Figure 7, in which the color represents

the velocity magnitude at the free surface. When the incident solitary wave impinges on the structure at the moment of  $t_1$ , the water surface in front of the structure rises abruptly due to the block of the structure. Meanwhile, the blocking effect also results in a reversing flow in front of the structure. The incident wave is separated from the two sides of the structure with a large magnitude of velocity. At the time of  $t_2$ , the rise of water surface at the structure front reaches its highest point, while the region of backwater in front of the structure expands. Afterwards, during the wave draw-down stage at the moment of  $t_3$ , the water surface elevation drops with the decrease in flow velocity. Finally, at the time of  $t_4$  during the wave trailing stage, the incoming solitary wave has almost fully passed through the structure, forming a thin-layer flow with low velocity.

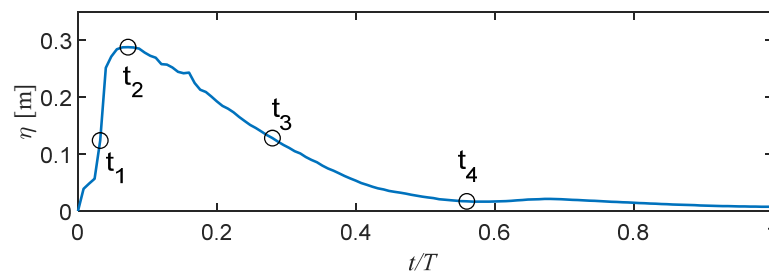


Figure 6. Time history of water surface elevation in front of the structure.

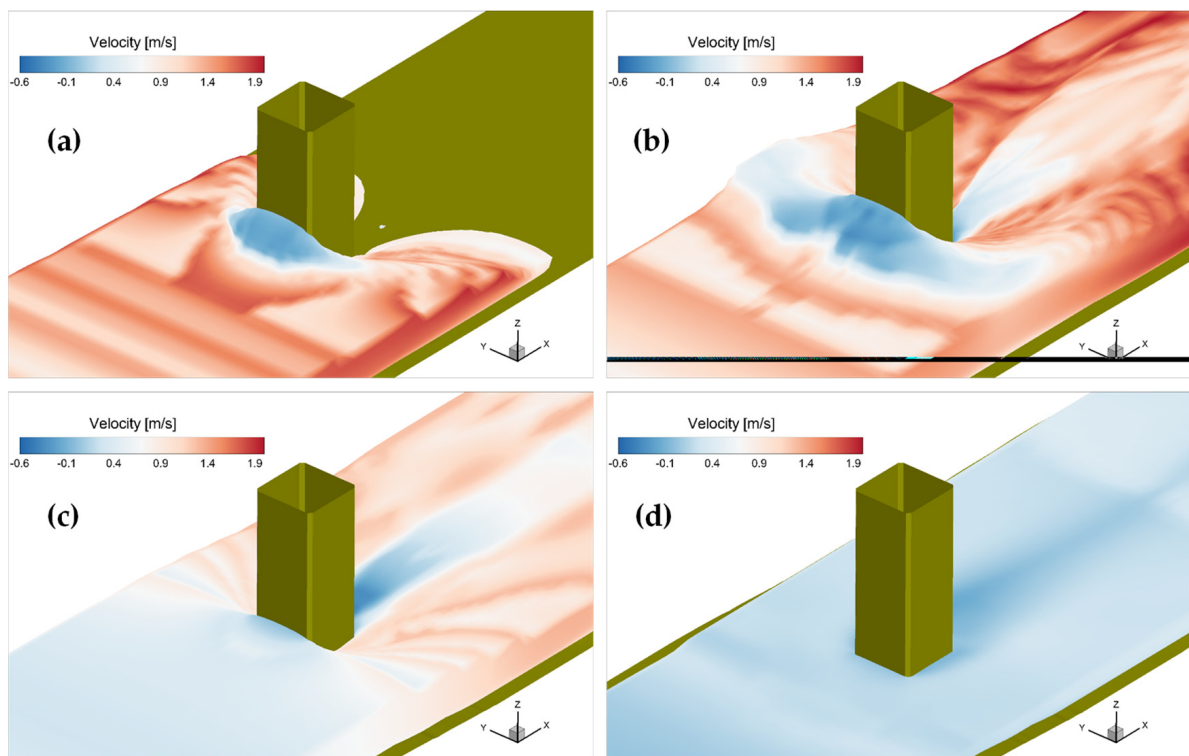
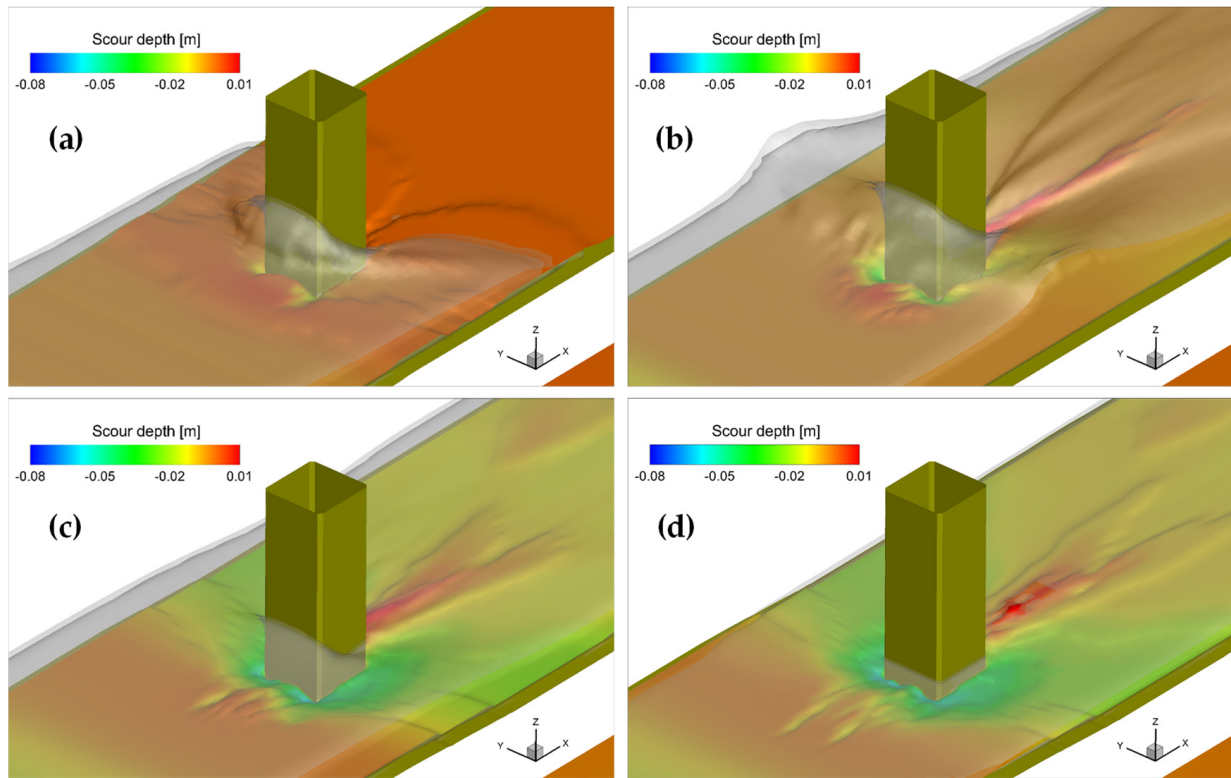


Figure 7. Simulated free surface flow features around structure at the moments of (a)  $t_1$ , (b)  $t_2$ , (c)  $t_3$ , and (d)  $t_4$ .

Figure 8 provides the evolution of the scour morphology around the structure during the wave inundation process. It obviously shows that the scour first occurred at the front corner of the structure. The reason is that the near-bed velocity at the front corner increases significantly due to flow separation downstream of the structure. Consequently, the bed scour occurs due to the amplified bed shear stress, and more sediment is transported, making the bed scour becomes more obvious. In addition to the bed shear stress (the primary driving force for sediment movement), the vortex induced by the flow separation

works as a vacuum to sweep the sediment suspension, which also contributes to the bed scour. The local scour area around the structure gradually extends and reaches its largest at the time of  $t_3$ , and the transported sediment is deposited behind the structure, causing bed accumulation. To better appreciate the above-described features, one video of the free surface and scour evolution process around the structure is provided (see Supplementary Video S1).



**Figure 8.** Simulated scour morphology around structure at the moments of (a)  $t_1$ , (b)  $t_2$ , (c)  $t_3$ , and (d)  $t_4$ .

#### 4.2. Wave Force on the Structure

Regarding the wave force acting on the structure, previous relevant studies have mainly focused on rigid-bed cases without considering the effect of scour. Figure 9 illustrates the difference in the wave force when considering scour versus ignoring scour. Note that the rigid-bed simulation (i.e., ignoring scour) is conveniently realized by turning off the sediment and morphological model. The comparison indicates that the wave force considering the scour is relatively larger, with the value of peak force being approximately 20% higher than that in the corresponding rigid-bed case. This finding means that: (i) the normally used wave force estimation method, employed without considering bed scour, would result in under-prediction; and (ii) the bed scour not only undermines the foundation stability but also causes a larger wave force on the structure. It should be admitted that, for the present case, the water inundation depth is low ( $<0.3$  m), and, correspondingly, the scour depth ( $\approx 0.1$  m) has a significant influence on the wave force. This finding is illuminating, as it implies that the scour effect needs to be considered in the prediction of the wave force on the structure, especially for the shallow-water scour scenario.

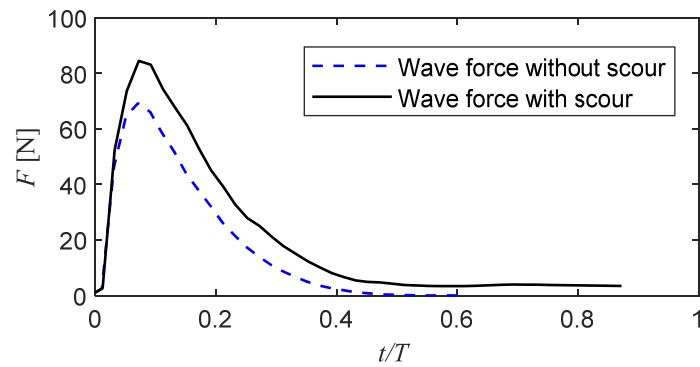


**Figure 9.** Comparison of wave force on the structure mounted on the rigid bed and scoured bed.

To identify the reason for the increase in the wave force under bed scour conditions, the vertical flow field at the symmetry plane of the structure is inspected, as shown in Figure 10. The comparison shows that the difference in the flow fields mainly lies in the near-bed flow. Figure 10c presents the vertical profiles of the velocity  $u$  in front of the structure at the peak force time, which confirms that the near-bed flow velocity for the scour case is larger than that for the corresponding rigid-bed case (see the region highlighted by the red box). The negative value of  $u$  near the bottom is found in the rigid-bed case due to the formation of a reverse flow in front of the structure. This can be illustrated from the horizontal flow field around the structure at the plane near the bed (Figure 11), which indicates that the reverse flow is more obvious in the rigid-bed case. In general, the flow velocity  $u$  at the structure front directly influences the hydrodynamic force on the structure, and the bed scour results in an increase in  $u$  and, consequently, an increase in the wave force.

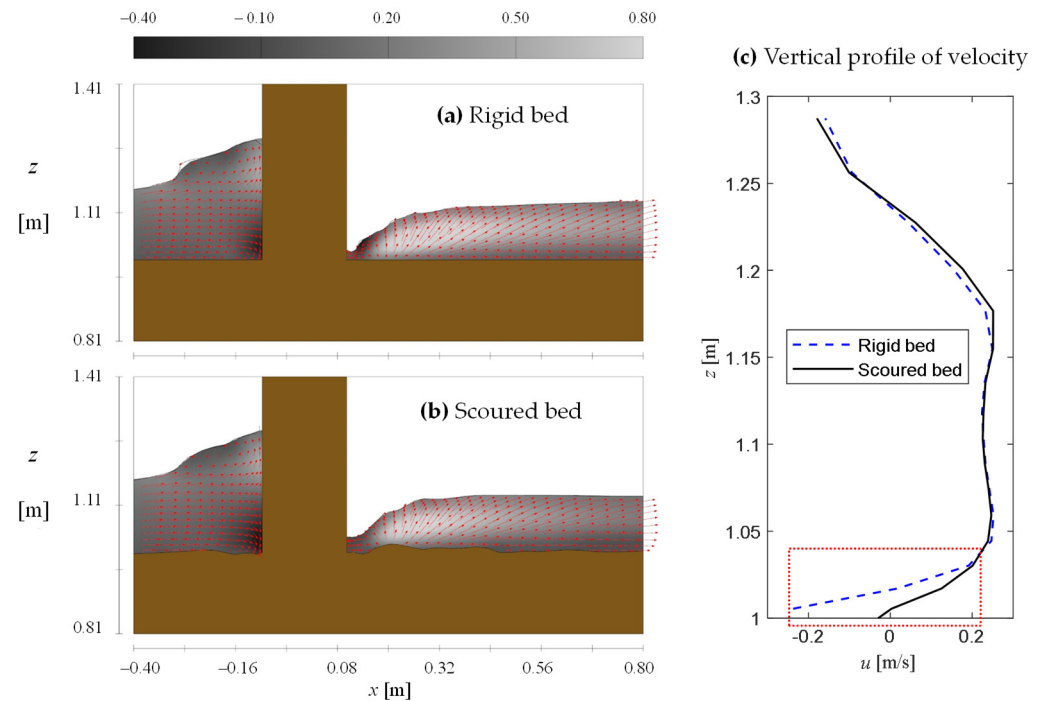


**Figure 10.** Comparisons of flow field and velocity profile between rigid-bed and scour-bed conditions: (a,b) vertical flow field at the symmetry plane of structure; (c) vertical profiles of velocity  $u$  in front of the structure.

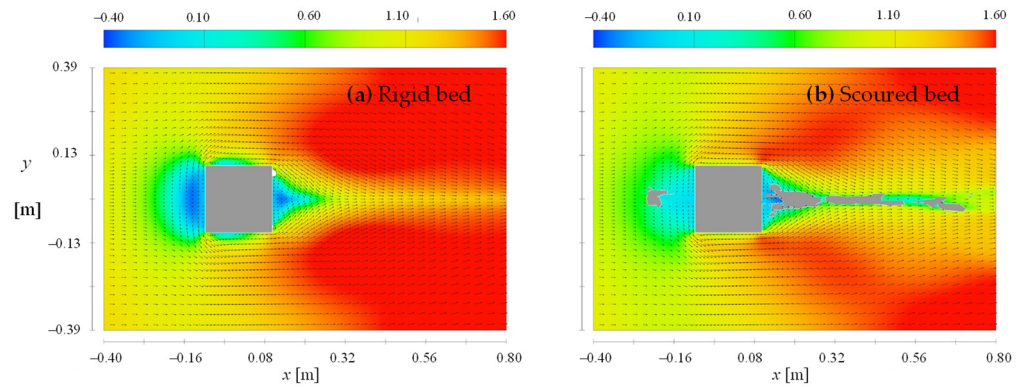


**Figure 11.** Horizontal flow field around the structure at the plane near the bottom bed under the conditions of (a) rigid bed and (b) scoured bed.

### 4.3. Scour Depth Development

Figure 12 shows the temporal development of the scour depth at the front and side positions of the structure. The front position is selected at the symmetry line of the front face, and the side position is selected at the front corner of the structure. The scour process is generally divided into three stages. At the early stage (Stage I, at the first  $0.2 T$ ), the scour depth increases quickly, which can be seen from the high scour rate demonstrated in Figure 12b. During the middle stage (Stage II, between  $0.2 T$  and  $0.5 T$ ), the fluctuation characteristics of the scour depth are found, and the scour depth reaches its maximum at the end of this stage. At the late stage (Stage III, at the late  $0.5 T$ ), the scour depth stops increasing, with even a slight deposition, and the scour depth keeps almost constant to the end. In other words, the scour process is almost completed by the end of the first half of the wave period. In addition, Figure 12 also shows that the scour at the side position is initiated earlier than the scour at the structure front, and the scour depth at the structure side is generally greater during the whole process.

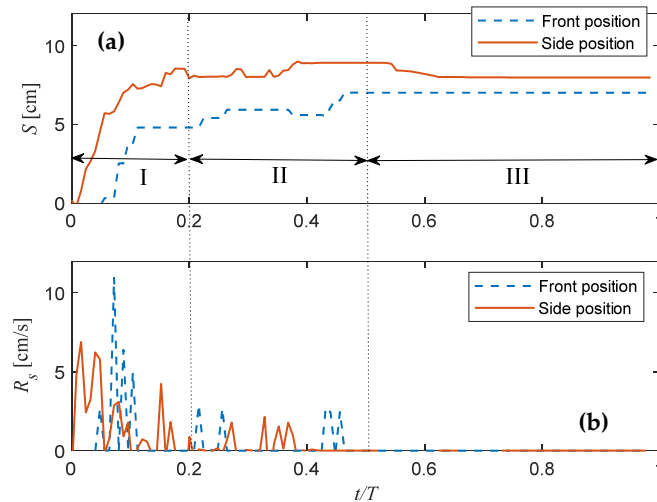


**Figure 12.** Temporal development of (a) scour depth and (b) scour rate at the front and side positions of the structure.

Figure 13 provides a comprehensive comparison by putting the variations of flow, sediment, and scour characteristics together for the purpose of elucidating the scouring mechanism. Note that the flow velocity  $U$ , kinetic energy  $k$ , and sediment concentration  $c$  are selected at a point close to the bottom bed. The temporal variations in terms of  $U$ ,  $k$ , and  $c$  between the front and side positions are distinctly different. For the side position of the structure, the temporal variations of the flow, sediment, and scour related variables are generally consistent during the wave inundation process, with almost identical times

of peak value. This is expected, as the scouring is an interaction process between flow, sediment, and bed; specifically, the enhancement of flow characteristics (e.g.,  $u$  and  $k$ ) leads to more sediment transport and the resultant bed scour. In contrast, the variations in flow and sediment are rather different at the front position of the structure. The value of  $u$  and  $k$  is generally small, which means that the driving force for sediment transport is very weak. This implies that the scour at the structure front is not due to the enhancement of local flow intensity, which is different from the scour mechanism at the structure side. Through the inspection of the scouring process around the structure, it is found that the scour is first formed at the front corner of the structure. Afterwards, the scour area gradually evolves to the front position, and the scour at the structure front starts to develop. Meanwhile, the vortex within the scour hole could also contribute to the scour development. Therefore, it is further confirmed that the scour at the front corner of the structure is the origin of the scour hole. This finding is also useful from the perspective of scour protection, as it means that some effective countermeasures for scour mitigation need to be set at the front corner of the structure.

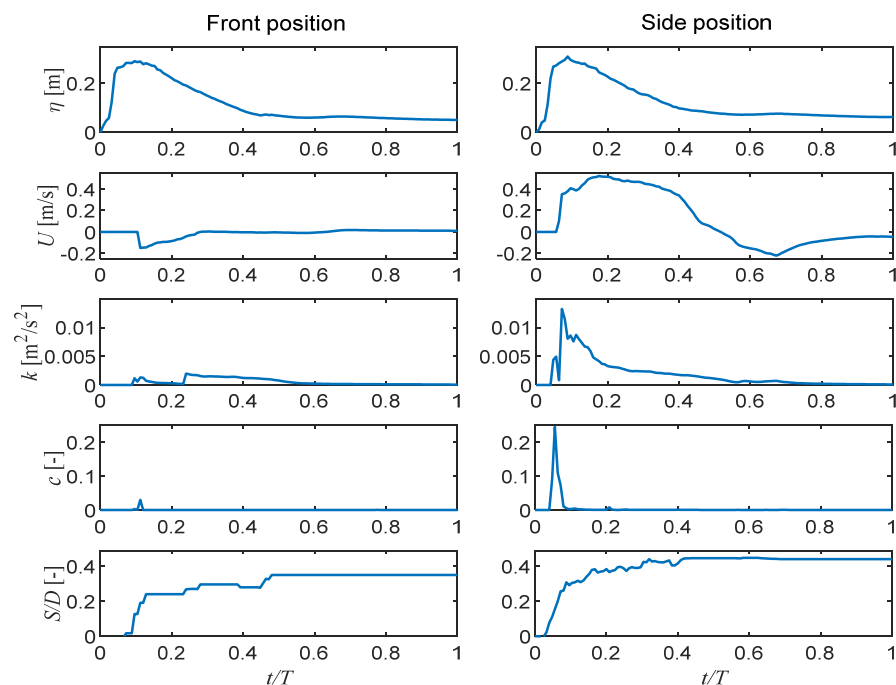


**Figure 13.** Comprehensive comparison of different variables development at the front and side positions of the structure.

#### 4.4. Comparison with Prediction Equation

From the point of view of practical application, some simple models (e.g., empirical equations) are more feasible for predicting the scour development. The most widely-used equation for predicting the temporal development of the scour depth can be expressed as an exponential function:

$$\frac{S}{S_f} = 1 - \exp\left[-\left(\frac{t}{T_s}\right)\right] \tag{19}$$

where  $S$  is the scour depth,  $S_f$  is the final scour depth, and  $T_s$  is the time scale of the scour calculated by integrating the scour curve [27]:

$$T_s = \int_0^{t_m} \frac{S_m - S}{S_m} dt \tag{20}$$

where  $S_m$  is the maximum scour depth at any given time and  $t_m$  is the time at which the maximum scour occurs.

Figure 14 shows the comparison between the scour depth development predicted by the equation and the CFD simulated results. In the figure, the time  $t$  is normalized by

$$t^* = \frac{\sqrt{g(s-1)d_{50}^3}}{D^2} t \tag{21}$$

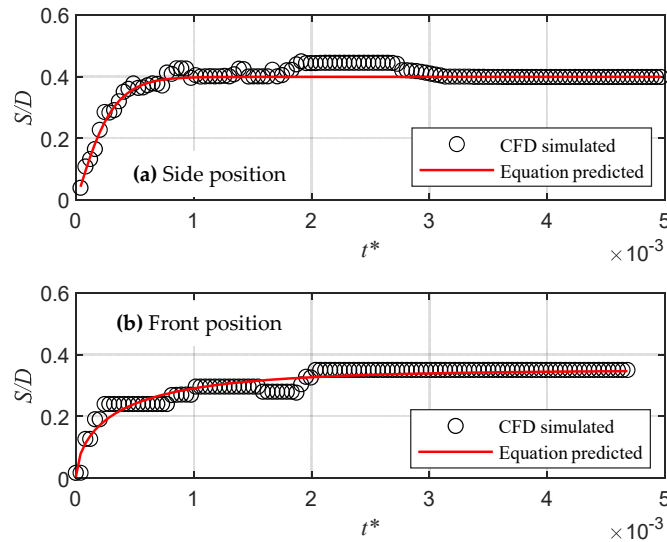


Figure 14. Comparison of scour depth development between the equation predicted and CFD simulated results at the (a) side and (b) front positions of the structure.

This demonstrates that the simple empirical equation performs well in predicting the scour depth development. In order to further validate the empirical equation, other experimental data from Pandey et al. (2017) [28] are collected, and the comparisons are plotted in Figure 15. The detailed conditions for the experiment are listed in Table 2. As can be seen from Figure 15, the present simple equation does a good job of predicting the scour depth development. However, it is worth noting that the simple equation mentioned above only considers the continual scouring condition; the fluctuating feature or even the slight deposition is not considered. Regarding this point, Link et al. (2020) [29] proposed a more complex predictive equation that considers the bed deposition due to sediment backfilling, and the interested readers can refer to their studies.

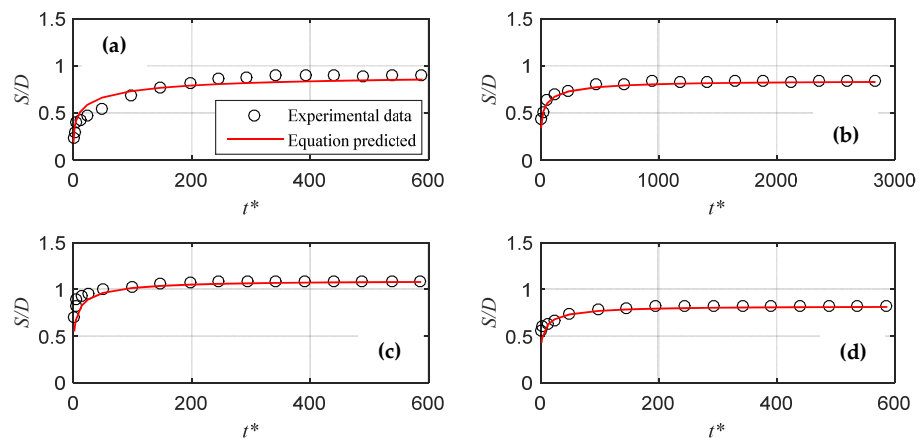


Figure 15. Comparison of temporal scour depth development predicted by the present equation against the experimental data from [28]: (a–d) Test 1–4.

**Table 2.** Experimental conditions from [28] used for validation.

Test No.	$D$ (m)	$U_0$ (m/s)	$h$ (m)	$d_{50}$ (mm)	$Re_D$	$Fr_D$	$d_{50}/D$
1	0.135	0.74	0.125	10.7	99,000	0.643	0.079
2	0.115	0.53	0.1	8.6	60,400	0.499	0.075
3	0.135	0.7	0.13	8.6	93,700	0.609	0.064
4	0.115	0.7	0.1	4.38	79,800	0.659	0.038

Note:  $D$  is cylinder diameter;  $U_0$  is approach flow velocity;  $h$  is flow depth;  $d_{50}$  is sediment median size;  $Re_D = U_0 D / \nu$ ;  $Fr_D = U_0 / (gD)^{0.5}$ .

## 5. Conclusions

In this study, a numerical modeling of flow and scour around a square onshore structure exposed to a solitary wave is conducted. The numerical simulation is based on a CFD model incorporating hydrodynamic, sediment transport, and morphological models. The hydrodynamic model is based on RANS equations coupled with the  $k-\omega$  turbulence model. The sediment model considers both the bed load and the suspended load transport, and the morphological model is based on a sediment continuity equation. The CFD model is validated through comparison with the available experimental data from a large-scale flume test. Based on the validated simulation results, some hydrodynamic and scour characteristics observed during the process of wave inundation of the structure are described and discussed in detail, and the main findings are:

- (1) The present CFD model can well reproduce the flow and scour characteristics around the structure, except for the scour depth development at the early stage. This is due to the limitations of RANS model as well as to the fact that the sediment transport model does not consider the effect of turbulence.
- (2) The scour starts at the front corner of the structure, which is also the position of the maximum scour depth. This is due to the enhancement of bed shear stress induced by the flow separation, and the scour area gradually extends to the front position of the structure.
- (3) Bed scour results in an increase in the wave force on the structure compared to the rigid-bed case without scour, which needs to be considered in the estimation of wave force, especially for the shallow-water scour scenario.
- (4) The scour depth develops rapidly at the early stage, with a high scour rate, and the scour process is almost completed in the first half of the wave period. A practical equation can be used to predict the temporal development of the scour depth.

**Supplementary Materials:** The following supporting information can be downloaded at: <https://www.mdpi.com/article/10.3390/jmse11010198/s1>, Video S1: Scour.avi.

**Author Contributions:** Conceptualization, J.L.; methodology, J.L. and J.H.; software, J.L.; validation, J.L.; formal analysis, J.L.; writing—original draft preparation, J.L.; writing—review and editing, J.L. and X.K.; visualization, Y.Y.; supervision, X.K.; project administration, R.J.; funding acquisition, J.L., X.K., Y.Y. and J.H. All authors have read and agreed to the published version of the manuscript.

**Funding:** This research is financially supported by the National Natural Science Foundation of China (Grant No. 52108137, 52008160, 52108186, and 52108434), the Natural Science Foundation of Hunan Province (Grant No. 2022JJ40065 and 2022JJ40620), and the China Postdoctoral Science Foundation (Grant No. 2021M701163).

**Institutional Review Board Statement:** Not applicable.

**Informed Consent Statement:** Not applicable.

**Data Availability Statement:** The data presented in this study is available from the corresponding author upon request.

**Acknowledgments:** The authors thank the editors and anonymous reviewers for their constructive comments to improve this paper.

**Conflicts of Interest:** The authors declare no conflict of interest.

## References

1. Bricker, J.D.; Francis, M.; Nakayama, A. Scour depths near coastal structures due to the 2011 Tohoku tsunami. *J. Hydraul. Res.* **2012**, *50*, 637–641. [[CrossRef](#)]
2. Chen, J.; Huang, Z.; Jiang, C.; Deng, B.; Long, Y. Tsunami-induced scour at coastal roadways: A laboratory study. *Nat. Hazards* **2013**, *69*, 655–674. [[CrossRef](#)]
3. Chen, J.; Jiang, C.; Yang, W.; Xiao, G. Laboratory study on protection of tsunami-induced scour by offshore breakwaters. *Nat. Hazards* **2016**, *81*, 1229–1247. [[CrossRef](#)]
4. Sumer, B.M.; Kirca, V.S.O. Scour and liquefaction issues for anchors and other subsea structures in floating offshore wind farms: A review. *Water Sci. Eng.* **2021**, *15*, 3–14. [[CrossRef](#)]
5. Li, J.; Fuhrman, D.R.; Kong, X.; Xie, M.; Yang, Y. Three-dimensional numerical simulation of wave-induced scour around a pile on a sloping beach. *Ocean. Eng.* **2021**, *233*, 109174. [[CrossRef](#)]
6. Sumer, B.M.; Sen, M.B.; Karagali, I.; Ceren, B.; Fredsøe, J.; Sottile, M. Flow and sediment transport induced by a plunging solitary wave. *J. Geophys. Res. Ocean.* **2011**, *116*, C01008. [[CrossRef](#)]
7. McGovern, D.J.; Todd, D.; Robinson, T.; Whitehouse, R.J.S.; Monaghan, J.; Gomes, E. Experimental observations of tsunami induced scour at onshore structures. *Coast. Eng.* **2019**, *152*, 103505. [[CrossRef](#)]
8. Mehrzad, R.; Nistor, I.; Rennie, C. Scour mechanics of a tsunami-like bore around a square structure. *J. Waterw. Port Coast. Ocean. Eng.* **2022**, *148*, 04021048. [[CrossRef](#)]
9. Xu, J.; Sun, J.; Shi, J.; Li, G.; Wang, X.; Ding, D.; Wang, C.; Wu, L. Increased wave load on the Gudong seawall caused by seabed scour. *Ocean. Eng.* **2022**, *250*, 111005. [[CrossRef](#)]
10. McGovern, D.J.; Robinson, T.; Chandler, I.D.; Allsop, W.; Rossetto, T. Pneumatic long-wave generation of tsunami-length waveforms and their runup. *Coast. Eng.* **2018**, *138*, 80–97. [[CrossRef](#)]
11. Afzal, M.S.; Bihs, H.; Kamath, A.; Arntsen, Ø.A. Three-dimensional numerical modeling of pier scour under current and waves using level-set method. *J. Offshore Mech. Arct. Eng.* **2015**, *137*, 032001. [[CrossRef](#)]
12. Baykal, C.; Sumer, B.M.; Fuhrman, D.R.; Jacobsen, N.G.; Fredsøe, J. Numerical simulation of scour and backfilling processes around a circular pile in waves. *Coast. Eng.* **2017**, *122*, 87–107. [[CrossRef](#)]
13. Zhang, Q.; Zhou, X.; Wang, J. Numerical investigation of local scour around three adjacent piles with different arrangements under current. *Ocean Eng.* **2017**, *142*, 625–638. [[CrossRef](#)]
14. Ahmad, N.; Bihs, H.; Myrhaug, D.; Kamath, A.; Arntsen, Ø.A. Three-dimensional numerical modelling of wave-induced scour around piles in a side-by-side arrangement. *Coast. Eng.* **2018**, *138*, 132–151. [[CrossRef](#)]
15. Le Quééré, P.A.; Nistor, I.; Mohammadian, A. Numerical modeling of tsunami-induced scouring around a square column: Performance assessment of FLOW-3D and Delft3D. *J. Coast. Res.* **2020**, *36*, 1278–1291. [[CrossRef](#)]
16. Bordbar, A.; Sharifi, S.; Hemida, H. Investigation of the flow behaviour and local scour around single square-shaped cylinders at different positions in live-bed. *Ocean Eng.* **2021**, *238*, 109772. [[CrossRef](#)]
17. Gautam, S.; Dutta, D.; Bihs, H.; Afzal, M.S. Three-dimensional Computational Fluid Dynamics modelling of scour around a single pile due to combined action of the waves and current using Level-Set method. *Coast. Eng.* **2021**, *170*, 104002. [[CrossRef](#)]
18. Hu, R.; Wang, X.; Liu, H.; Chen, D. Numerical study of local scour around tripod foundation in random waves. *J. Mar. Sci. Eng.* **2022**, *10*, 475. [[CrossRef](#)]
19. Li, J.; Kong, X.; Yang, Y.; Deng, L.; Xiong, W. CFD investigations of tsunami-induced scour around bridge piers. *Ocean Eng.* **2022**, *244*, 110373. [[CrossRef](#)]
20. Lu, Y.; Wang, Z.; Yin, Z.; Wu, G.; Liang, B. Experimental and numerical studies on local scour around closely spaced circular piles under the action of steady current. *J. Mar. Sci. Eng.* **2022**, *10*, 1569. [[CrossRef](#)]
21. Xu, J.; Xia, J.; Wang, L.; Zhu, H.; Avital, E.J. Direct numerical simulation on local scour around the cylinder induced by internal solitary waves propagating over a slope. *Ocean Eng.* **2022**, *247*, 110525. [[CrossRef](#)]
22. Lai, Y.G.; Liu, X.F.; Bombardelli, F.A.; Song, Y. Three-dimensional numerical modeling of local scour: A state-of-the-art review and perspective. *J. Hydraul. Eng.* **2022**, *148*, 0312202. [[CrossRef](#)]
23. Zhao, M. A Review on recent development of numerical modelling of local scour around hydraulic and marine structures. *J. Mar. Sci. Eng.* **2022**, *10*, 1139. [[CrossRef](#)]
24. Wilcox, D.C. *Turbulence Modeling for CFD*, 3rd ed.; DCW Industries, Inc.: La Canada, CA, USA, 2006.
25. Song, Y.; Xu, Y.; Liu, X. Physically based sand slide method in scour models based on slope-limited diffusion. *J. Hydraul. Eng.* **2020**, *146*, 04020074. [[CrossRef](#)]
26. Li, J.; Qi, M.; Fuhrman, D.R.; Chen, Q. Influence of turbulent horseshoe vortex and associated bed shear stress on sediment transport in front of a cylinder. *Exp. Therm. Fluid Sci.* **2018**, *97*, 444–457. [[CrossRef](#)]
27. Larsen, B.E.; Fuhrman, D.R.; Baykal, C.; Sumer, B.M. Tsunami-induced scour around monopile foundations. *Coast. Eng.* **2017**, *129*, 36–49. [[CrossRef](#)]

28. Pandey, M.; Sharma, P.K.; Ahmad, Z.; Singh, U.K. Evaluation of existing equations for temporal scour depth around circular bridge piers. *Environ. Fluid Mech.* **2017**, *17*, 981–995. [[CrossRef](#)]
29. Link, O.; Garcia, M.; Pizarro, A.; Alcayaga, H.; Palma, S. Local scour and sediment deposition at bridge piers during floods. *J. Hydraul. Eng.* **2020**, *146*, 04020003. [[CrossRef](#)]

**Disclaimer/Publisher’s Note:** The statements, opinions and data contained in all publications are solely those of the individual author(s) and contributor(s) and not of MDPI and/or the editor(s). MDPI and/or the editor(s) disclaim responsibility for any injury to people or property resulting from any ideas, methods, instructions or products referred to in the content.